RSC Advances

ROYAL SOCIETY OF CHEMISTRY

www.rsc.org/advances

A sustainable nitrogen- and oxygen-doped carbon sheet was prepared from pigskin for supercapacitors with high capacitance and excellent rate capability.

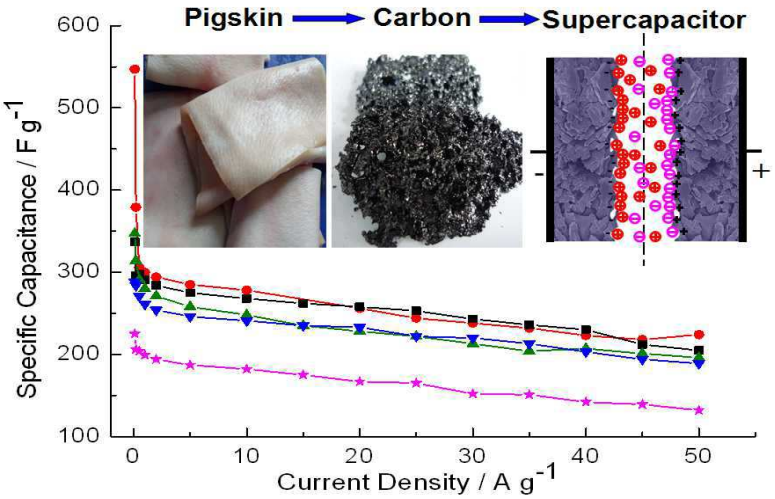

Cite this: DOI: 10.1039/c0xx00000x

www.rsc.org/xxxxxx

ARTICLE TYPE

Preparation of novel pigskin-derived carbon sheets and their low-temperature activation-induced high capacitive performance

Yong Wang, Ru Yang,* Yuan Wei, Zijian Zhao and Min Li

Received (in XXX, XXX) Xth XXXXXXXXX 20XX, Accepted Xth XXXXXXXXX 20XX

DOI: 10.1039/b000000x

Nitrogen- and oxygen-doped carbon sheets are prepared by carbonization and KOH-activation of a collagen-rich biomass resource pigskin and employed as supercapacitor electrodes. The porosity and surface chemistry are tailored through controlling activation temperature from 600 to 900 °C, and the specific surface area and nitrogen content vary between 2209 and 3337 m^2 g^{-1} and between 0.65 and 3.77 wt%, respectively. A considerable oxygen content ranging from 8.39 to 12.28 at% is also attained. The sample activated at 600 °C exhibits an exceptional specific capacitance of up to 547 F g^{-1} in 6 M KOH due to abundant effective micropores and high heteroatom content, which induce high double-layer capacitance and additional pseudocapacitance, respectively. Furthermore, pigskin-derived carbon shows excellent high rate performance with specific capacitance of 278 F g^{-1} at 10 A g^{-1} and 224 F g^{-1} at 50 A g^{-1} and good cycling stability (93% retention at 2 A g^{-1} after 10000 cycles).

Introduction

Electrochemical double layer capacitors (EDLC) are environmentally friendly energy storage devices working through accumulating/releasing charged ions in the double layer formed at the interface between electrode and electrolyte.[1] EDLC provides rapid charge-discharge performance, high power delivery or uptake, and extremely long cycle life, required by expanding applications such as hybrid electrical vehicles, pulse laser technique, memory back-up systems and other portable electronics.[2-5] The performance of EDLC strongly depends on the characteristics of electrode materials, such as surface area, pore structure, surface chemistry and so forth.[1,3] Electrode materials of EDLC widely studied include activated carbons, carbon aerogels, carbon onions, carbon nanotubes and graphene, among which activated carbons are employed as the preferred material in commercial EDLC due to their large specific surface area, tunable porosity, chemical stability and moderate cost.[5-8] The development of superior activated carbons with excellent capacitive performance is becoming one of the most attractive research interests.

In the past years, great efforts have gone into promoting the capacitance of activated carbon electrodes.[9-16] One of the most direct ways is to achieve a considerably large surface area that generates extensive electrode/electrolyte interface for charge storage.[13-16] However, the study also found that the specific capacitance increased non-linearly with the specific surface area of activated carbons.[17] Some samples with a surface area of even over 3000 m^2 g^{-1} showed a much smaller specific capacitance (<10 μF cm^{-2}) than the theoretical value (15-25 μF cm^{-2}), since partial surface of ultramicropores could not be effectively utilized as a result of pore size and wettability limitation.[1,18] Therefore, improving the capacitance just by increasing the porosity is experiencing a bottleneck, and complementary approaches are required when large surface area and appropriate pore size distribution are simultaneously considered.

Recently, studies have shown that modification of surface chemistry by incorporating heteroatoms such as O, N, S, P and B can significantly enhance the capacitance of carbon electrodes.[19-24] Especially N-doped carbon has become a sparkling research spot.[25] Nitrogen functionalities on carbon can not only induce additional pseudocapacitance but also strengthen the surface wettability, both conducing to a high capacitance.[5,26,27] Traditionally, the principal routes to introduce nitrogen to activated carbons include post-treatment with nitrogenous compounds at elevated temperature, and in-situ doping by carbonization of nitrogenous precursors.[28] Post-treatment may result in a lower surface area and less developed porous structure, and can not incorporate nitrogen atoms into the inner carbon network. In-situ doping using nitrogenous precursors can enable homogeneous nitrogen incorporation with a controlled chemistry, and simultaneously realize a large surface area after an appropriate activation process. Synthetic polymers (urea formaldehyde resins, polyaniline, polypyrrole, etc.) and nitrogen-rich ionic liquids are common nitrogenous precursors studied.[22,29-31] But with the decreasing availability of fossil energy and increasing demand for renewable resource, alternative raw materials should be urgently explored for high-performance N-doped activated carbons.

From the viewpoint of sustainable chemistry, biomass undoubtedly becomes the first-choice substitute because it is abundant, renewable and economical. Plant-based precursors have proved to be eligible for activated carbons,[32] while most of them are eclipsed in producing N-doped carbons because of

insufficient nitrogen. Researchers then shift their focus on some nitrogen-rich animal by-products containing extremely substantial protein. For example, Li et al. prepared mesoporous nitrogen-rich carbons from egg protein and 3D-architectural carbons from chicken eggshell membranes, which exhibited excellent specific capacitances of 390 F g^{-1} and 297 F g^{-1} in aqueous electrolytes, respectively.[33,34] Jin's group reported a silk-derived microporous carbon nanoplates with a specific capacitance of 264 F g^{-1} in 1 M H_2SO_4 electrolyte.[35] A chicken feather-derived carbon was reported to display a high initial specific capacitance of 302 F g^{-1} in 1 M H_2SO_4.[36] A porous carbon derived from endothelium corneum gigeriae galli exhibited a capacitance of 198 F g^{-1} in 6 M KOH.[37] Interestingly, several groups even found human hair a good precursor for N-doped carbon used as supercapacitor electrodes.[38-40] These cases indicate that nitrogenous biomass is paving a promising direction for preparation of N-doped carbon, and new biomass-derived carbons with better performance need to be intensively studied.

Herein, we prepare novel sheet-like N- and O-doped carbons from natural pigskin, more easily to collect than eggshell membranes and hair, less costly than silk and egg protein, and most importantly showing high capacitive properties. As an animal by-product, crude pigskin comprises approximately 60-75% water, 21%-23% protein, 10% fat and other trace minerals.[41] Pigskin proteins are mainly collagen, fibers or fiber bundles of which form a three-dimensional network structure in dermal tissues.[42] Every year, we get meat from 1.3 billion pigs globally, while pigskin has not been well utilized except for a fraction of 20%-30% being made into leather products.[43,44] Some of them are used to extract collagen protein, but more are discarded as kitchen waste. Considering about 48% carbon, 14% nitrogen, 28% oxygen, 6% hydrogen, and 0.16% sulfur in dry pigskin, it is possible and meaningful to produce high-added carbon materials with heteroatoms from this natural feedstock. In this study, effects of activation temperature on the porosity and surface chemistry of pigskin-derived activated carbon (PSAC) are comprehensively investigated. The high specific surface area, plentiful nitrogen and oxygen functionalities, and suitable pore size distribution make the carbons exhibit outstanding capacitive behaviors, including high specific capacitance, exceptional rate capability and good cycle stability. These materials possess potential advantages for application in supercapacitors with high energy and power density.

Experimental

Preparation of materials

Commercial raw pigskin was obtained from Carrefour Beijing Chuangyijia Store, and fat tissue was scraped off with a scalpel. The pigskin was cut into 1×1 cm pieces and degreased in 1 M $NaHCO_3$ solution at 37 °C for 10 h. After washed to neutral, pigskin pieces were ultrasonicated in ethanol for 30 min and dried at 80 °C for 24 h. The clean and dry pigskin was carbonized in a tube furnace at 600 °C for 2 h under a nitrogen atmosphere. The carbonized product was ground and sieved (80-120 mesh), and then mixed with KOH at weight ratio of 1:4.5. The mixture was further activated in N_2 at different temperatures (600, 650, 700, 800 and 900 °C) for 3.5 h, respectively. The resultant product was washed with 1 M HCl solution and deionized water, and finally dried at 80 °C. Pigskin-derived activated carbon was denoted as PSAC-*T*, where *T* represented the activation temperature.

Characterization

The morphology of products was examined using a Hitachi S-4700 scanning electron microscope (SEM) at 5-20 kV and a JEOL JEM-3010 transmission electron microscope (TEM) at 200 kV. Energy dispersive X-ray (EDX) measurement was performed with a spectrometer attached to JEM-3010. Nitrogen adsorption-desorption (77 K) analysis was carried out on a Micromeritics ASAP 2020 surface area and porosity analyzer. Samples were degassed at 300 °C under vacuum for 12 h prior to measurement. Brunauer-Emmett-Teller (BET) and density functional theory (DFT) methods were used to calculate the specific surface area and pore size distribution. Fourier transform infrared spectra (FTIR) were obtained with a Nicolet 8700 FTIR spectrometer by averaging 256 scans in the 4000-400 cm^{-1} spectral range at 4 cm^{-1} resolution. Elemental analysis was performed on an Elementar vario EL CUBE. X-ray photoelectron spectroscopy (XPS) was used to determine the surface atomic composition of carbons. XPS spectra were taken on a Thermo VG ESCALAB 250 spectrometer equipped with a monochromatic Mg Kα X-ray source (1253.6 eV). X-ray diffraction (XRD) was conducted using a Rigaku D/MAX-2500 with Cu Kα radiation. Raman spectra were measured with a Renishaw in Via Micro-Raman Spectroscopy System at 514 nm.

Electrochemical measurements

Electrodes were prepared from pigskin-derived activated carbon by coating a mixture of 80 wt% of carbon sample, 10 wt% of acetylene black and 10 wt% of polytetrafluoroethylene (PTFE) to a nickel foam, and then dried at 80 °C for 24 h. Eight mg of activated carbon on each nickel foam was used. The electrochemical measurements were performed in 6 M KOH aqueous solution using a three-electrode system with an above electrode, a Pt sheet and a Hg/HgO as the working, counter and reference electrodes, respectively. Cyclic voltammetry (CV) and electrochemical impedance spectroscopy were recorded by a CHI 760E electrochemical workstation. The galvanostatic charge-discharge tests were carried out on a LAND CT2001A tester. The specific capacitance (*C*) in F g^{-1} was calculated from the discharge slop during galvanic cycling according to the equation: $C=I\Delta t/m\Delta V$, where *I* is the discharge current (A), Δt is the discharge time (s), *m* is the mass of active materials in the working electrode (g), and ΔV is the discharge potential change (V).

Results and discussion

Morphology and porosity

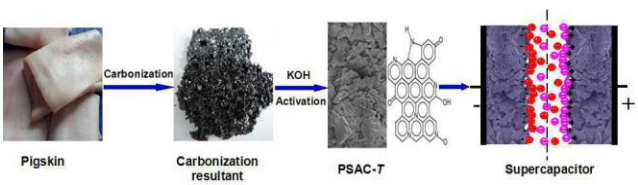

Fig. 1 Transformation of pigskin into N- and O-doped activated carbon sheets used in supercapacitors.

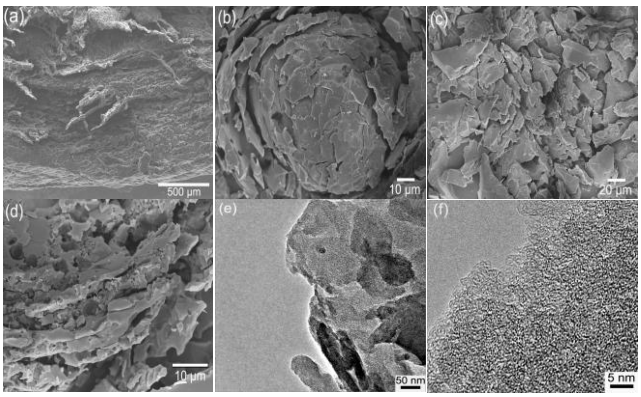

Fig. 2 SEM images of raw pigskin (a) and pigskin-derived carbon sheets activated at 600 °C (b, c, d), and HRTEM images (e, f).

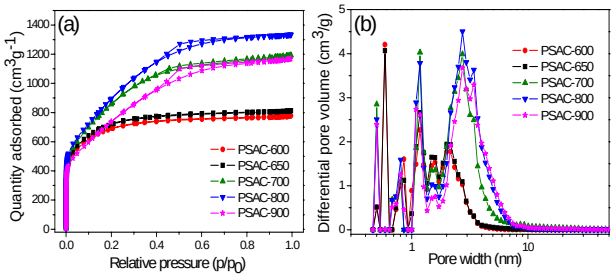

Fig. 3 Nitrogen (77 K) adsorption-desorption isotherms (a) and pore size distributions (b) of pigskin-derived carbon sheets activated at different temperatures.

Fig. 1 illustrates a schematic diagram for the preparation of pigskin-derived activated carbon materials. Crude pigskin was cleaned, dried and carbonized at first. The carbon resultant was mixed with KOH and activated at various temperatures. Finally, the N- and O-doped activated carbon could be applied in supercapacitors and other fields.

It is well known that pigskin is mainly composed of collagen fibers.[42] Fig. 2a shows the interwoven fiber bundles form a macroscopically disordered network structure in nature. These fibers have a rough surface with many protuberances of tens of micrometers in size (Fig. S1). After carbonization and activation, sheet-like carbon are generated (Fig. 2b). Most of carbon sheets shed from the bulky block and exhibit irregular polygons in shape with diameters of over 10 μm (Fig. 2c). There are some macroscopic pores on carbon sheets or between the plies as a result of KOH etching at 600 °C (Fig. 2d). The images of sample activated at 800 °C further reveal the macroscopic pore structure and rich nanopores (Fig. S2). Those macropores will act as ion-buffering reservoirs to reduce the electrolyte diffusion distances to the interior surfaces in the applications of EDLC.[45] TEM images (Fig. 2e-f) exhibit an amorphous porous structure with partially graphitic microstructure, implying good electrical conductivity of carbon sheets.[28] Selected-area EDX in Fig. S3 shows that oxygen and nitrogen are the main heteroatoms on carbon surface, and the nitrogen content detected is 3.3 wt% and 2.9 at% (a few micrometers in depth), indicating an evident nitrogen doping in this carbon.

Nitrogen adsorption-desorption isotherms and pore size distributions of as-prepared activated carbon sheets are shown in Fig. 3, and pore structure parameters are listed in Table S1. As shown in Fig. 3a, pigskin-based carbons activated at 600 and 650 °C present type I isotherms according to the IUPAC classification, indicating microporous materials. Whereas isotherms of the samples activated at 700, 800 and 900 °C belong to type IV, suggesting the presence of rich mesopores. For the latter three samples, the broad knees of adsorption curves imply wide pore size distributions. Fig. 3b reveals that the pore size of samples activated at relatively low temperatures ranges from 0.5 to 4 nm, while that of other samples activated over 700 °C is 0.5–8 nm. Obviously, a high temperature helps to enlarge the pores. As temperature increases, mesopore volume occupies 20, 21, 50, 57 and 59% of the total pore volume, respectively. Meanwhile, the specific surface area, total pore volume and average pore width all increase (Table S1) owing to the enhanced pore creation by KOH activation at higher temperatures. However, the micropore surface area and micropore volume decrease with rising temperature because of pore collapse resulting from the violent KOH etching. When activation temperature reaches 900 °C, PSAC-900 shows a dramatic decrease in specific surface area and micropores as well as mesopores, suggesting that an excessively high temperature will result in not only micropore reduction but also mesopore damage. PSAC-800 displays the largest specific surface area of 3337 $m^2 g^{-1}$, the greatest total pore volume of 2.06 $cm^3 g^{-1}$ and the most mesopores. PSAC-600 has the richest micropores that can enhance the electrical double layer, and especially has the most abundant micropores between 0.6 and 0.9 nm that proved to be optimal for EDLCs.[3] Thus, activation temperature plays a vital role in controlling the porosity of pigskin-derived activated carbons.

Surface chemistry

The surface chemistry of as-prepared samples was firstly studied by FTIR (Fig. 4a). As can be seen, one broad adsorption band at 3433 cm^{-1} is assigned to N-H or O-H stretching vibration, and two bands at 2924 and 2854 cm^{-1} are attributed to C-H stretching vibration.[46-48] The peak at 1621 cm^{-1} is ascribed to C=C stretching vibration in aromatic rings or the incompletely carbonized C=N.[49,50] The C=O stretching vibration may also be included around this peak. The weak peak at 1383 cm^{-1} is due to the characteristic C-N stretching vibration, confirming the presence of nitrogen species.[46,48] The band at 1092 cm^{-1} covers the C-O stretching vibration and C-H bending vibration.[47,48] The less intense band at around 798 cm^{-1} corresponds to the out-of-plane N-H deformation vibration.[49] Almost all the adsorption peaks of functional groups containing N, O and H heteroatoms get weak with increasing temperature. Anyhow, FTIR results preliminarily demonstrate the existence of N-H and C-N species in pigskin-based activated carbons.

The surface chemistry was further investigated by XPS measurements. XPS spectra of pigskin-derived activated carbons present N and O peaks on carbon surface (Fig. S4), which get weakened as temperature rises. The surface nitrogen contents of as-prepared samples calculated by XPS are 2.96, 2.45, 1.42, 0.69 and 0.65 at%, respectively, decreasing with increasing activation temperature (Table S2). The nitrogen atoms are identified as four types of chemical states (Fig. 4b-f): pyridinic N (N-6, 398.7±0.3 eV), pyrrolic and pyridone N (N-5, 400.3±0.3 eV), quaternary N

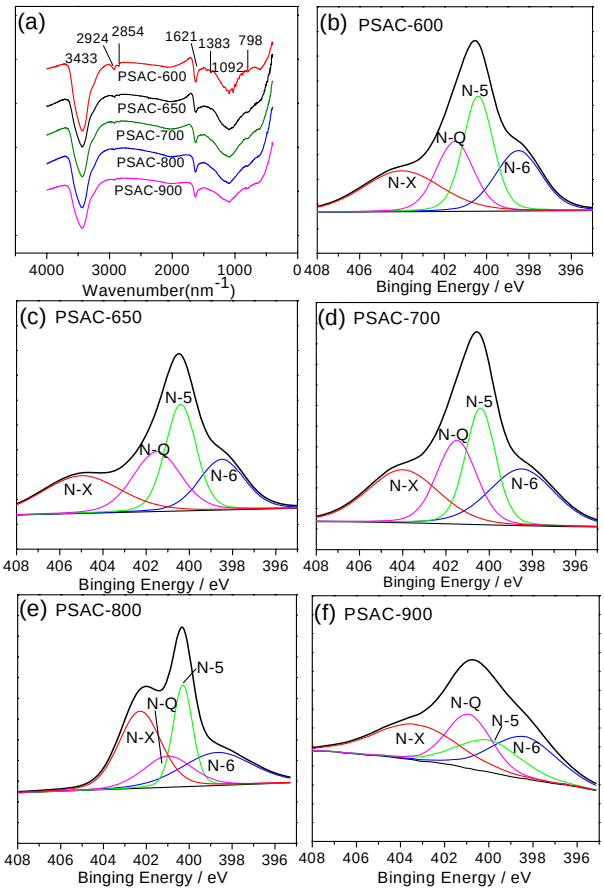

Fig. 4 FTIR (a) and N 1s XPS (b-f) spectra of pigskin-derived carbon sheets activated at different temperatures.

(N-Q, 401.4±0.5 eV) and pyridine-N-oxide (N-X, 402-405 eV).[28] Thereinto nitrogen located at the edge of graphite plane, such as N-6 and N-5, can trigger pseudocapacitance effects.[28,37] PSAC-600 presents the highest content of N-6 and N-5, about 65% of total surface nitrogen. An elevated temperature will bring about a corresponding decrease in these two nitrogen species. Elemental analysis (EA) is used to study bulk nitrogen content of as-prepared samples. It can be seen from Table S2 that bulk nitrogen content shows a similar variation to surface nitrogen, indicating that increasing activation temperature is adverse to total nitrogen retention in carbon. For PSAC-600, the nitrogen contents measured by EA and XPS are very close to that from EDX analysis, further ensuring the accuracy of results. Except for nitrogen, oxygen on carbon surface also deserves notice because some oxygen species contribute to pseudocapacitance as well. The oxygen atoms may come from the residual oxygen in the precursor and the introduced oxygen by KOH activation. Pigskin-derived activated carbons have an oxygen content of 12.28-8.39 at%, decreasing with the activation temperature (Table S2). O1s spectra are deconvoluted into three peaks at 531.5, 532.9 and 534.5 eV (Fig. S5), which represent carbonyl oxygen in quinones (O-I), carbonyl oxygen in esters and anhydrides or oxygen atoms in phenolic hydroxyl (O-II), and non-carbonyl oxygen in esters and anhydrides (O-III), respectively.[51] O-I species are considered to cause pseudocapacitance effects.[20] PSAC-600 possesses the most O-I and total N-6 and N-5 content, suggesting the highest pseudocapacitance in EDLC.

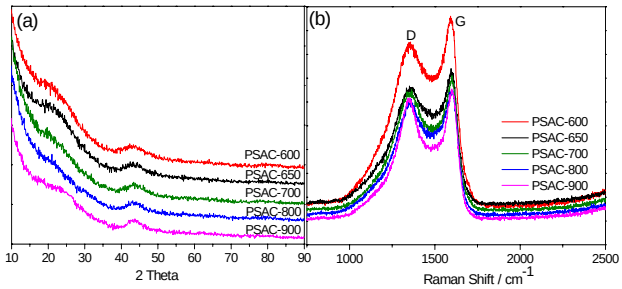

Fig. 5 XRD patterns (a) and Raman spectra (b) of pigskin-derived carbon sheets activated at different temperatures.

Physical structure

XRD patterns of as-prepared samples exhibit two broad diffraction peaks at around 2θ = 25° and 43° (Fig. 5a), corresponding to the reflection from the (002) plane and the overlapped reflections from the (100) and (101) planes, respectively.[35,52] A large intensity increase in the low-angle scatter is consistent with the presence of a high density of micropores.[35] The absence of a sharp peak reveals the predominantly amorphous structure. Compared with the carbonized resultant without activation (Fig. S6), the diffraction peaks obviously get weakened after activation, suggesting destruction of graphite layer alignment by KOH. As temperature increases from 600 to 800 °C, the peak intensity becomes even weaker due to the enhanced KOH etching. However, for the sample activated at 900 °C, the intensity of the two peaks turns a little stronger, indicating an improved graphitic crystallinity, probably because severe reactions between carbon and KOH quickly finish at a high temperature over 800 °C, and then the orderly rearrangement of graphite layers occurs.

Raman spectra (Fig. 5b) show two peaks at 1350 and 1592 cm^{-1} representing the D band and the G band, respectively.[27] The G band is a characteristic feature of graphitic layers and corresponds to the tangential vibration of carbon atoms, while the D band relates to disordered carbon or defective graphitic structures.[34] The intensity ratio of these two peaks (I_D/I_G) partially depends on the graphitization degree.[34] The higher the ratio, the lower the degree of graphitization.[27] Here, the intensity of these two bands gradually gets weaker with increasing activation temperature from 600 to 800 °C and then turns a little stronger at 900 °C. The I_D/I_G values are 0.878, 0.884, 0.908, 0.944 and 0.936, respectively, indicating a reduced graphitization degree resulting from the enhanced chemical activation from 600 to 800 °C. The graphitization degree slightly increases at 900 °C in accordance with XRD results. Both XRD and Raman analysis demonstrate that a high activation temperature will lead to a decrease in graphitization degree, which may further affect the conductivity of materials.

Electrochemical properties

Electrochemical performance of PSAC is evaluated in 6 mol L^{-1} KOH aqueous electrolyte in a three-electrode system. Cyclic voltammograms of as-prepared samples exhibit approximately rectangular shape from -0.8 to 0.2 V, indicating a dominant EDLC nature (Fig. 6a). There are obviously well-broadened redox humps at around -0.4 V representing the presence of pseudocapacitance induced by nitrogen and oxygen

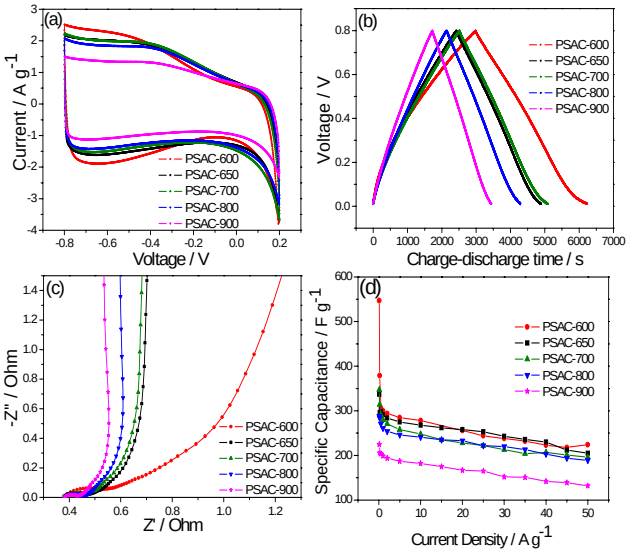

Fig. 6 Electrochemical performance of pigskin-derived carbon sheets in 6 M KOH. (a) Cyclic voltammetry curves at a scan rate of 5 mV s^{-1}; (b) galvanostatic charge-discharge curves at 0.1 A g^{-1}; (c) Nyquist plots; (d) specific capacitances at different current densities.

functionalities on carbon surface.[35,40] As activation temperature increases, the humps recede and CV curves become more regular rectangles, which is closely related to the decrease of heteroatomic groups, especially such as N6, N5 and O-I (Table S2). CV curves also exhibit sharp current leaps near the upper potential limit which could be attributed to charge-transfer from water decomposition with oxygen evolution. Additional charges from oxygen evolution reactions accumulating on carbon surface induce a high current. The sample activated at lower temperature and with more micropores has a more intense peak, suggesting the key contribution of micropores to charge storage. Galvanostatic charge-discharge curves deviate from a linear shape a little and show slightly distorted triangular patterns (Fig. 6b), also confirming the existence of pseudocapacitance. The high-temperature sample apparently tends to a more perfect triangular shape because of less heteroatoms. Nyquist plots in a frequency range from 10 kHz to 0.01 Hz are provided to study the electrochemical impedance behavior of PSAC (Fig. 6c). In the low-frequency region, the nearly vertical line represents the dominance of double-layer charge storage. The Warburg-type line (the slope of 45 °C portion) at high-to-medium frequency corresponds to ion diffusion resistance. The semicircle in the high-frequency range is associated with pseudocharge-transfer resistance.[28] PSAC-600 exhibits the highest diffusion resistance, as seen in its longest Warburg-type line, because it contains the most micropores and the least mesopores, which can hinder the diffusion of electrolyte ions through the pores. PSAC-600 also shows the largest semicircle, indicating a high pseudocharge-transfer resistance caused by the prominent pseudocapacitance. When activation temperature is raised, the resistance obviously decreases as a result of the enlarged pore width and the diminished heteroatoms. According to the XRD and Raman analysis, a high activation temperature should have resulted in a high resistance due to the decreasing conductivity, but actually the porosity and surface chemistry play dominant roles as compared with tiny variations in conductivity for these high-surface-area activated carbons.

The specific capacitance of PSAC-600 can reach 547 F g^{-1} calculated from the discharge curve at a constant current of 0.1 A g^{-1}, much higher than other as-prepared samples (Table S1). This value is quite close to the theoretical maximum according to the electric double layer capacitance of 15-25 μF cm^{-2} for activated carbons.[1] However, it is believed that such a high capacitance of PSAC-600 results from the combination of redox reactions and electrical double-layer formation. Especially the abundant nitrogen and oxygen functionalities leading to pseudocapacitive behavior and good wettability make great contributions to this high value. PSAC-800 with the largest surface area of 3337 m^2 g^{-1} shows a relatively low specific capacitance of 288 F g^{-1} probably because of its low nitrogen and oxygen content, small micropore volume and so forth. Previous literature has pointed out that when the surface area of some activated carbons reaches 3000 m^2 g^{-1}, the specific capacitance drops to less than 10 μF cm^{-1}, much smaller than the theoretical electric double layer value. Additionally, it is a common phenomenon that the specific capacitance of N- and O-rich carbon materials is mainly associated with the nitrogen and oxygen content rather than the specific surface area.[33] It is also found in this paper that the sample activated at lower temperature tends to have a better capacitive performance, suggesting low-temperature activation should be a worthwhile process to get doped carbons from animal by-products. For all the samples, a decrease in specific capacitance with the increase in current density can be observed (Fig. 6d) because electrolyte ions have inadequate time to diffuse into all inner pores of electrode materials at a high current density. The sample activated at a lower temperature displays a better rate capability because its more abundant micropores will bring about more double-layer capacitance. The specific capacitance of PSAC-600 dramatically decreases at the first several low current densities (0.1 A g^{-1}, 547 F g^{-1}; 0.2 A g^{-1}, 380 F g^{-1}; 0.5 A g^{-1}, 306 F g^{-1}) due to the attenuation of pseudocapacitance whose rate capability is inferior to double-layer capacitance.[28] Nevertheless, at the current density of 10 A g^{-1}, PSAC-600 maintains a high capacitance of 278 F g^{-1} owing to its plentiful micropores, which is superior to the aforementioned N-doped carbons.[33-40,50,51] Other samples activated at 650, 700, 800 and 900 °C show capacitances of 253, 248, 233 and 182 F g^{-1}, respectively, under the current load of 10 A g^{-1}. Even at 50 A g^{-1}, PSAC-600 still holds a high capacitance of 224 F g^{-1}, a satisfying result for supercapacitors based on carbon electrodes.

Galvanostatic charge-discharge curves of PSAC-600 at different current densities (Fig. 7a) depict that the charge-discharge time shortens with increasing current density, and rapid charge or discharge completes within only 3.6 s at 50 A g^{-1} with the curve still remaining as an approximately linear shape, indicating a fairly good rate performance. The rate performance is further investigated by CV tests at enhanced scan rates (Fig. 7b). A rectangular CV curve with a broad hump between -0.8 V and -0.4 V is shown when the scan rate is not higher than 20 mV s^{-1}. As scan rate over 50 mV s^{-1}, the curve is inclined to a distorted triangle-like shape caused by pseudocharge-transfer resistance and ion retardation within ultrafine micropores. The retardation results in a sluggish current response at a high scan rate, which

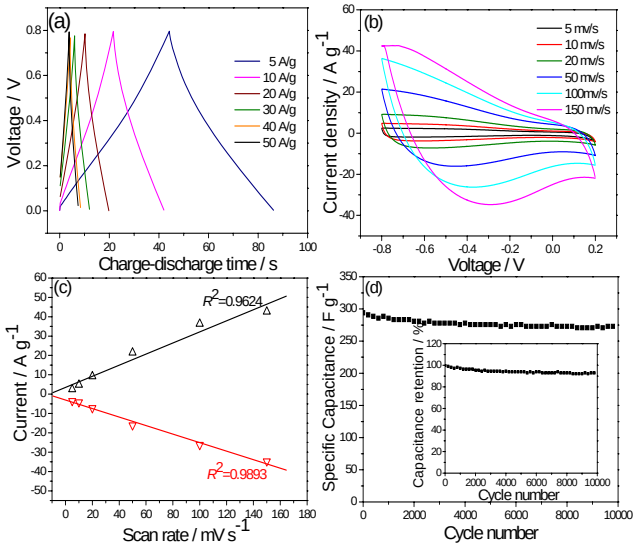

Fig. 7 Rate performance of pigskin-derived carbon sheets in 6 M KOH. (a) Charge-discharge curves of PSAC-600 at different current densities; (b) cyclic voltammetry curves of PSAC-600 at various scan rates; (c) the relationship between the peak current and the scan rate for PSAC-600; (d) cycling stability of PSAC-600 at a current load of 2 A g^{-1}.

can be intuitively observed from the relationship between the peak current and scan rate (Fig. 7c). The electrochemical cathodic and anodic peak currents of PSCA-600 display linear dependence on scan rate with the correlation coefficient less than 0.99. By contrast, PSAC-800 exhibits a rectanglar CV curve even at a high scan rate of 250 mV s^{-1}, and its correlation coefficient of peak current–scan rate plots is more than 0.99 (Fig. S7), suggesting a less impeded charge-transfer. More mesopores and less nitrogen and oxygen heteroatoms are considered to play a positive part in rapid charge-discharge process for PSAC-800. Noteworthily, although lacking mesopores and having excessive redox reactions may induce side effects on rate performance of PSAC-600, the richest micropores leading to an enhancement of electric double layer capacitance can compensate for these defects even at a high rate. The long-term cycling stability is very essential for EDLC, especially for those with pseudocapacitance. The cycle life of PSAC-600 is measured under a current load of 2 A g^{-1} (Fig. 7d). After 2500 cycles, a specific capacitance of 281 F g^{-1} remains with 4.4% attenuation, and after 10000 cycles, the capacitance loss is only 7.1%, indicating a good stability.

Conclusions

Nitrogen- and oxygen-doped activated carbon sheets with large surface area have been first prepared from pigskin by KOH activation. Tunable pore structure and surface chemistry have been achieved through controlling the activation temperature, which can further affect the electrochemical property of pigskin-derived carbon. A higher temperature results in a larger specific surface area and mesopore volume but a smaller micropore volume and a lower heteroatom content. The sample activated at 600 °C displays an exciting capacitance of up to 547 F g^{-1} due to the combination of double layer capacitance and prominent pseudocapacitance induced by the most abundant micropores and the richest nitrogen and oxygen functionalities. It also shows an excellent rate capability (224 F g^{-1} at 50 A g^{-1}) and good cycling stability (7.1% loss after 10000 cycles at 2 A g^{-1}). Suitable pore size distribution and sufficient nitrogen and oxygen functionalities play more important roles than just a high surface area in improving the capacitance. Pigskin should be a potentially sustainable precursor for preparation of nitrogen-containing porous carbons used in supercapacitors and other advanced energy devices (such as fuel cells and lithium ion batteries) as well as heterogeneous catalysis.

Acknowledgements

We greatly acknowledge the financial support by the National Natural Science Foundation of China (51372012).

Notes and references

State Key Laboratory of Chemical Resource Engineering, Beijing Key Laboratory of Electrochemical Process and Technology for Materials, Beijing University of Chemical Technology, Beijing, P. R. China. Fax: +86 10 64436736; Tel: +86 10 64436736; E-mail: ruyang@mail.buct.edu.cn

† Electronic Supplementary Information (ESI) available: SEM image of pigskin surface; SEM and HRTEM images of PSAC-800; EDS; Full XPS and O1s XPS spectra of five samples; XRD pattern of pigskin-derived carbon without activation; cyclic voltammetry curves at various scan rates, the relationship between the peak current and the scan rate for PSAC-800, and tables. See DOI: 10.1039/b000000x/

1 B.E. Conway, *Electrochemical supercapacitors: scientific fundamentals and technological applications*, Kluwer Academic/Plenum, New York, 1999.
2 W. Xing, C.C. Huang, S.P. Zhuo, X. Yuan, G.Q. Wang, D. Hulicova Jurcakova, Z.F. Yan and G.Q. Lu, *Carbon*, 2009, **47**, 1715
3 P. Simon and Y. Gogotsi, *Nat. Mater.*, 2008, **7**, 845.
4 J.R. Miller and P. Simon, *Science*, 2008, **321**, 651.
5 Y. Zhai, Y. Dou, D. Zhao, P.F. Fulvio, R.T. Mayes and S. Dai, *Adv. Mater.*, 2011, **23**, 4828.
6 L.L. Zhang and X.S. Zhao, *Chem. Soc. Rev.*, 2009, **38**, 2520.
7 S.L.Candelaria, Y. Shao, W. Zhou, X. Li, J. Xiao, J.-G. Zhang, Y. Wang, J. Liu, J. Li and G. Cao, *Nano Energy*, 2012, **1**, 195.
8 W. Gu and G. Yushin, *WIREs Energy Environ.*, 2013, doi:10.1002/wene.102.
9 L.F. Chen, X.D. Zhang, H.W. Liang, M. Kong, Q.F. Guan, P. Chen, Z.Y. Wu and S.H. Yu, *ACS Nano*, 2012, **6**, 7092.
10 L.F. Chen, Z.H. Huang, H.W. Liang, W.T. Yao, Z.Y. Yu and S.H. Yu, *Energy Environ. Sci.*, 2013, **6**, 3331.
11 L.F. Chen, Z.H. Huang, H.W. Liang, Q.F. Guan and S.H. Yu *Adv. Mater.*, 2013, **25**, 4746.
12 L.F. Chen, Z.H. Huang, H.W. Liang, H.L. Gao and S.H. Yu *Adv. Funct. Mater.*, 2014, doi: 10.1002/adfm.201400590.
13 O. Barbieri, M. Hahn, A. Herzog and R. Kötz, *Carbon*, 2005, **43**, 1303.
14 B. Xu, S. Hou, G. Cao, M. Chu and Y. Yang, *RSC Adv.*, 2013, **3**, 17500.
15 P.A. Goodman, H. Li, Y. Gao, Y.F. Lu, J.D. Stenger-Smith and J. Redepenning, *Carbon*, 2013, **55**, 291.
16 K. Karthikeyan, S. Amaresh, S.N. Lee, X. Sun, V. Aravindan, Y.-G. Lee and Y.S. Lee, *ChemSusChem*, 2014, **7**, 1435.
17 T.E. Rufford, D. Hulicova-Jurcakova, E. Fiset, Z. Zhu and G.Q. Lu, *Electrochem. Commun.*, 2009, **11**, 974.
18 E. Raymundo-Piñero, K. Kierzek, J. Machnikowski and F. Béguin, *Carbon*, 2006, **44**, 2498.
19 H. Guo and Q. Gao, *J. Power Sources*, 2009, **186**, 551.
20 D. Hulicova-Jurcakova, M. Seredych, G.Q. Lu and T.J. Bandosz, *Adv. Funct. Mater.*, 2009, **19**, 438.
21 J.P. Paraknowitsch and A. Thomas, *Energy Environ. Sci.*, 2013, **6**, 2839.

22 C. Wang, L. Sun, Y. Zhou, P. Wan, X. Zhang and J. Qiu, *Carbon*, 2013, **59**, 537.
23 X.Y. Chen, C. Chen, Z.J. Zhang, D.H. Xie, X. Deng and J.W. Liu, *J. Power Sources*, 2013, **230**, 50.
24 G. Hasegawa, M. Aoki, K. Kanamori, K. Nakanishi, T. Hanada and K. Tadanaga, *J. Mater. Chem.*, 2011, **21**, 2060.
25 K.N. Wood, R. O'Hayre and S. Pylypenko, *Energy Environ. Sci.*, 2014, **7**, 1212.
26 S.L. Candelaria, B.B. Garcia, D. Liu and G. Cao, *J. Mater. Chem.*, 2012, **22**, 9884.
27 M. Zhou, F. Pu, Z. Wang and S. Guan, Carbon, 2014, 68, 185.
28 B. Xu, S. Hou, G. Cao, F. Wu and Y. Yang, *J. Mater. Chem.*, 2012, **22**, 19088.
29 L. Li, E. Liu, J. Li, Y. Yang, H. Shen, Z. Huang, X. Xiang and W. Li, *J. Power Sources*, 2010, **195**, 1516.
30 L. Wei, M. Sevilla, A.B. Fuertes, R. Mokaya and G. Yushin, *Adv. Funct. Mater*., 2012, **22**, 827.
31 T.-P. Fellinger, A. Thomas, J. Yuan and M. Antonietti, *Adv. Mater.*, 2013, **25**, 5838.
32 Y.-J. Kim, B.-J. Lee, H. Suezaki, T. Chino, Y. Abe, T. Yanagiura, K.C. Park and M. Endo, *Carbon*, 2006, **44**, 1592.
33 Z. Li, L. Zhang, B.S. Amirkhiz, X. Tan, Z. Xu, H. Wang, B.C. Olsen, C.M.B. Holt and D. Mitlin, *Adv. Energy Mater.*, 2012, **2**, 431.
34 Z. Li, Z. Xu, X. Tan, H. Wang, C.M.B. Holt, T. Stephenson, B.C. Olsen and D. Mitlin, *Energy Environ. Sci.*, 2013, **6**, 871.
35 Y.S. Yun, S.Y. Cho, J. Shim, B.H. Kim, S.-J. Chang, S.J. Baek, Y.S. Huh, Y. Tak, Y.W. Park, S. Park and H.-J. Jin, *Adv. Mater.*, 2013, **25**, 1993.
36 Q. Wang, Q. Cao, X. Wang, B. Jing, H. Kuang and L. Zhou, *J. Power Sources*, 2013, **225**, 101.
37 X. Hong, K.S. Hui, Z. Zeng, K.N. Hui, L. Zhang, M. Mo and M. Li, *Electrochim. Acta*, 2014, **130**, 464.
38 W. Si, J. Zhou, S. Zhang, S. Li, W. Xing and S. Zhuo, *Electrochim. Acta*, 2013, **107**, 397.
39 Z. Guo, Q. Zhou, Z. Wu, Z. Zhang, W. Zhang, Y. Zhang, L. Li, Z. Cao, H. Wang and Y. Gao, *Electrochim. Acta*, 2013, **113**, 620.
40 W. Qian, F. Sun, Y. Xu, L. Qiu, C. Liu, S. Wang and F. Yan, *Energy Environ. Sci.*, 2014, **7**, 379.
41 S. Zhao and G. Li, *Leather Chem*. (in Chinese), 2006, **23**, 19.
42 X. Dai, L. Wang, K. Ma, B. Liu, H. Li and K. Pan, *J. Med. Biolo. Eng.*, 2013, **33**, 221.
43 K.L. Stephen, *Life cycle assessment of UK pig production systems: the impact of dietary protein source*, University of Edinburgh, MPhil thesis, 2012.
44 H. Yang and Z. Shu, *J. Chem. Pharm. Res*., 2014, **6**, 683.
45 F. Xu, R. Cai, Q. Zeng, C. Zou, D. Wu, F. Li, X. Lu, Y. Liang and R. Fu, *J. Mater. Chem.*, 2011, **21**, 1970.
46 M. Sevilla, P. Valle-Vigón and A.B. Fuertes, *Adv. Funct. Mater.*, 2011, **21**, 2781.
47 X. Fan, L. Zhang, G. Zhang, Z. Shu and J. Shi, *Carbon*, 2013, **61**, 423.
48 Z.L. Wu, P. Zhang, M.X. Gao, C.F. Liu, W. Wang, F. Leng and C.Z. Huang, *J. Mater. Chem. B*, 2013, **1**, 2868.
49 G.-P. Hao, W.-C. Li, D. Qian and A.-H. Lu, *Adv. Mater.*, 2010, **22**, 853.
50 X. Liu, L. Zhou, Y. Zhao, L. Bian, X. Feng and Q. Pu, *ACS Appl. Mater. Interfaces*, 2013, **5**, 10280.
51 B. Xu, H. Duan, M. Chu, G. Cao and Y. Yang, *J. Mater. Chem. A*, 2013, **1**, 4565.
52 F. Su, C.K. Poh, J.S. Chen, G. Xu, D. Wang, Q. Li, J. Lin and X.W. Lou, *Energy Environ. Sci.*, 2011, **4**, 717.